ACS APPLIED MATERIALS & INTERFACES

www.acsami.org

Research Article

Spectrally and Spatially Selective Emitters Using Polymer Hybrid Spoof Plasmonics

Gil Ju Lee,[‖] Do Hyeon Kim,[‖] Se-Yeon Heo, and Young Min Song*

Cite This: *ACS Appl. Mater. Interfaces* 2020, 12, 53206−53214

Read Online

ACCESS | Metrics & More | Article Recommendations | Supporting Information

ABSTRACT: Optimized thermal emitters using optical resonances have been attracting increased attention for diverse applications, such as infrared (IR) sensing, thermal imaging, gas sensing, thermophotovoltaics, thermal camouflage, and radiative cooling. Depending on the applications, the recently developed IR devices have been tailored to achieve not only spectrally engineered emission but also spatially resolved emission using various nanometallic structures, metamaterials, and multistacking layers, which accompany high structural complexity and prohibitive production cost. Herein, this article presents a simple and affordable approach to obtain spatially and spectrally selective hybrid thermal emitters (HTEs) based on spoof surface plasmons of microscaled Ag grooves manifested in encapsulation polymer layers. Theoretical analyses found that the polymer hybrid plasmonics allows diverse emission tuning within the long-wave IR (LWIR; 8−14 μm) region as follows: (1) spatially selective emission peaks only exist in the interface of Ag grooves and IR-transparent layers and (2) near-unity spectrally selective emission is obtained by refining inherent emissivity of a thin IR-opaque layer. Also, parametric studies computationally optimized the structural parameters for spatially and spectrally selective HTEs. Using the optimized parameters, the authors fabricated two HTEs and demonstrated the intriguing emission features in terms of infrared data encoding/decoding and radiative cooling, respectively. These successful demonstrations open up the applicability of HTEs for tailoring IR emission in a spatially and spectrally selective manner.

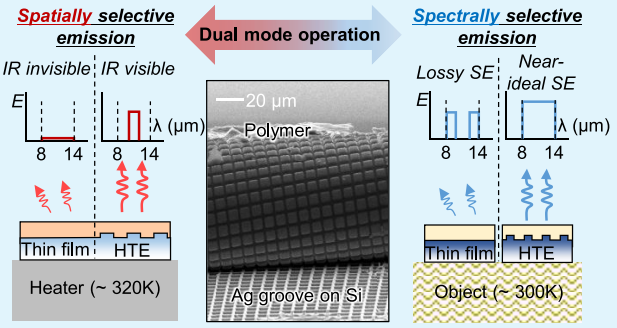

KEYWORDS: *infrared emitters, selective emitters, spoof surface plasmon, radiative cooling, infrared data encoding/decoding*

1. INTRODUCTION

A broad spectrum of Planck's blackbody radiation over a wide range of wavelengths is used for various applications. The emission control of such incandescent sources in the infrared (IR) region is of paramount importance in applications that require different wavelength-selective emission features, for instance, narrowband emissions for thermophotovoltaics,[1−5] gas detection,[6−9] and biosensing,[10] and wideband emissions for thermography use ranging from everyday life to industrial applications.[11] In particular, thermal detection/imaging devices operate within one of the three major atmospheric transmission windows (ATWs): short-wave IR (SWIR; 0.7−2.5 μm), mid-wave IR (MWIR; 3−5 μm), and long-wave IR (LWIR; 8−14 μm) to avoid strong absorption by dust, greenhouse gases, and water vapor.[12,13]

Among them, the LWIR window has the highest usage because LWIR imaging involves ambient-temperature objects (i.e., ∼ 300 K) to extremely hot objects (i.e., > 2000 K).[14] Furthermore, passive radiative cooling, which is an eco-friendly energy-saving technique, is a representative application of the LWIR window owing to its broadband transparency and strong radiation at ambient temperatures simultaneously.[15−18] In addition to the spectrally optimized applications, spatially resolved emission controls have been used for infrared displays[19] and anticounterfeiting technologies.[20,21]

Over the past few decades, various design rules have been provided to satisfy the abovementioned needs for spectral and spatial thermal emission control in nano-/microphotonic structures, including metallic nanostructures,[2,3,5,22−26] metamaterials,[27−30] and multistacking layers.[31−34] However, there remain challenges such as high structural complexity,[35,36] prohibitive production cost,[21,37,38] and weak emissivity.[39] Here, we present a simple and affordable approach for spectrally and spatially selective emitters using a polymer hybrid spoof surface plasmon (sSP). The proposed hybrid thermal emitter (HTE) consists of a Ag corrugated pattern on a Si substrate and an IR-transparent or IR-opaque encapsulating layer on a Ag groove. Since emissivity engineering is intertwined with the encapsulation layer, the HTE can function

Received: July 21, 2020
Accepted: October 29, 2020
Published: November 10, 2020

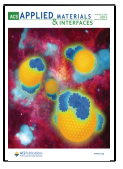

https://dx.doi.org/10.1021/acsami.0c13177
ACS Appl. Mater. Interfaces 2020, 12, 53206−53214

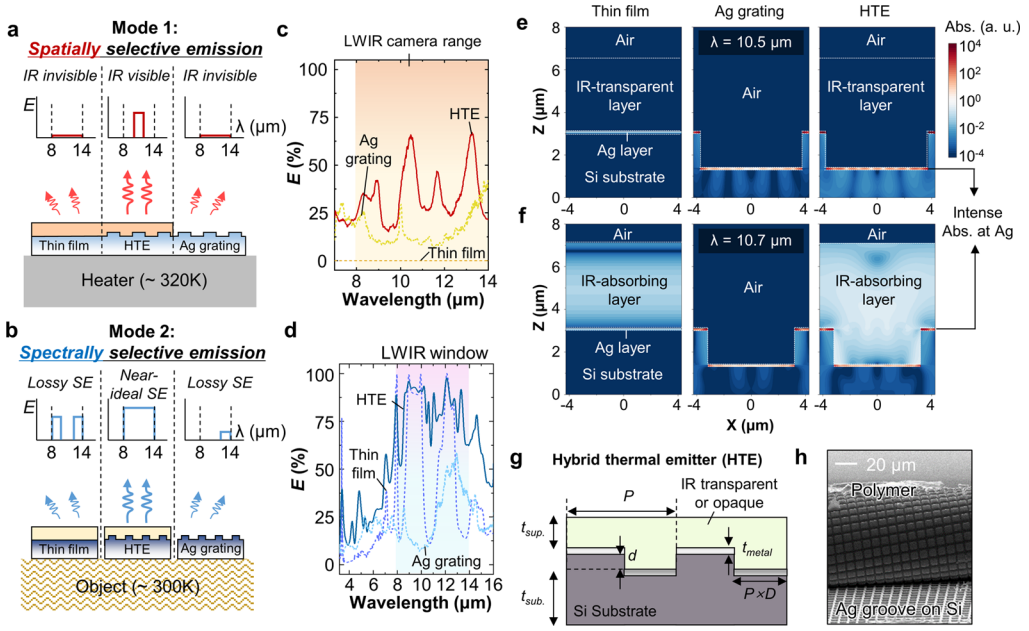

Figure 1. Spatially and spectrally selective emitters using polymer hybrid spoof surface plasmons. (a,b) Schematic illustrations of the HTEs working in two modes (i.e., spatially and spectrally selective emission modes) through (a) emissivity rearrangement and (b) refinement by introducing IR-transparent and IR-absorbing layers, respectively, on a corrugated silver pattern. In each mode, the hybridization of the corrugated pattern and IR-transparent/absorbing layers modulates the desired emissivity spectra in the LWIR range. (c,d) Simulated emissivity spectra for (c) spatially and (d) spectrally selective HTEs with control groups such as a Ag grating and thin-film emitters. (e,f) Cross-sectional absorption profiles for (e) spatially and (f) spectrally selective emission modes at the wavelengths of 10.5 and 10.7 μm: (left) thin film, (center) Ag grating, and (right) HTE. "Abs." means absorption. (g) Illustration for the structural parameters of the HTE. The parameters are period—P, depth—d, duty cycle—D, substrate thickness—t_{sub}, superstrate thickness—t_{sup}, and metal thickness—t_{metal}. (h) SEM image of a partially unglued HTE.

in two operating forms: mode 1—spatially selective emission using an IR-transparent layer and mode 2—spectrally selective emission using an IR-absorbing layer. The presented HTEs for the two modes are theoretically designed, experimentally fabricated, and successfully demonstrated in the form of IR data encoding/decoding, where the encoded pattern is only viewable within a specific area, and radiative cooling, where thermal energy is released by a near-unity selective emission in the LWIR window.

2. RESULTS AND DISCUSSION

2.1. Theoretical and Computational Analysis for HTE Design Guidelines. *2.1.1. Hybrid Thermal Emitters for Spatially and Spectrally Selective Emissions.* Our proposed HTEs have two operating modes, namely, mode 1—spatially selective emission with an IR-transparent layer (Figure 1a) and mode 2—spectrally selective emission with an IR-absorbing layer (Figure 1b) that work within the LWIR window. Simulation results for each structure demonstrate the detailed emissivity spectra (Figure 1c,d). In mode 1, only the Ag grating and the IR-transparent thin film exhibit unnoted emissivity spectra (i.e., IR invisible; Figure 1c; orange and yellow dashed curves), whereas the Ag grating with an IR-transparent film (i.e., HTE for mode 1) shows remarkable emissivity enhancement (Figure 1c; red solid curve). Although "mode 1" is based on emissivity tuning, the synergy of the grating and the IR-transparent superstrate permits the spatially resolved selective emission feature.

In mode 2, a thin polydimethylsiloxane (PDMS) film, which is an IR-absorbing material, presents a prominent selective emission, but it has large emissivity loss (i.e., lossy selective emitter; SE, Figure 1d; blue dashed line). Only the Ag grating case shows a negligible emissivity curve likewise mode 1, that is, low emissivity (Figure 1d; sky-blue dashed line). However, the Ag grating with an IR-absorbing film (i.e., HTE for mode 2) demonstrates a near-unity selective emission in the LWIR regime (Figure 1d; blue solid line).

To investigate the detailed emissivity enhancement phenomena, the absorption profiles are simulated because absorption could be equal to emissivity by Kirchhoff's law (Figure 1e,f). In mode 1, weak absorption is found at the Ag layer in the thin-film structure (Figure 1e; left). Without an encapsulation layer, the Ag grating absorbs the photons, but the intensity is considerably low (Figure 1e; center). HTE with an IR-transparent layer exhibits strong absorption at the Ag layer and enhanced absorption in the Si substrate (Figure 1e; right). In mode 2, the thin-film layer absorbs more incident photons than the Ag layer (Figure 1f; left). Only the Ag grating case displays a similar tendency with the case of mode 1 (Figure 1f; center). HTE with an IR-absorbing layer also exhibits intense absorption at the Ag layer, but absorption in the IR-absorbing layer is increased compared to that of the thin film; hence, both absorption enhancements ameliorate emissivity more (Figure 1f; right).

The structural parameters of the HTEs are illustrated in Figure 1g, and the notations are as follows: period—P, depth—d, duty cycle—D, substrate thickness—t_{sub}, superstrate thickness—t_{sup}, and metal thickness—t_{metal}. The geometrical parameters for each mode are as follows: (1) mode 1: P = 10 μm, d = 1.7 μm, D = 75%, t_{sub} = 500 μm, t_{metal} = 100 nm, and t_{sup} = 3.5 μm, and (2) mode 2: P = 8 μm, d = 1.7 μm, D = 75%, t_{sub} = 500 μm, t_{metal} = 100 nm, and t_{sup} = 4 μm. The scanning electron microscopy (SEM) image displays a partially unglued

https://dx.doi.org/10.1021/acsami.0c13177
ACS Appl. Mater. Interfaces 2020, 12, 53206−53214

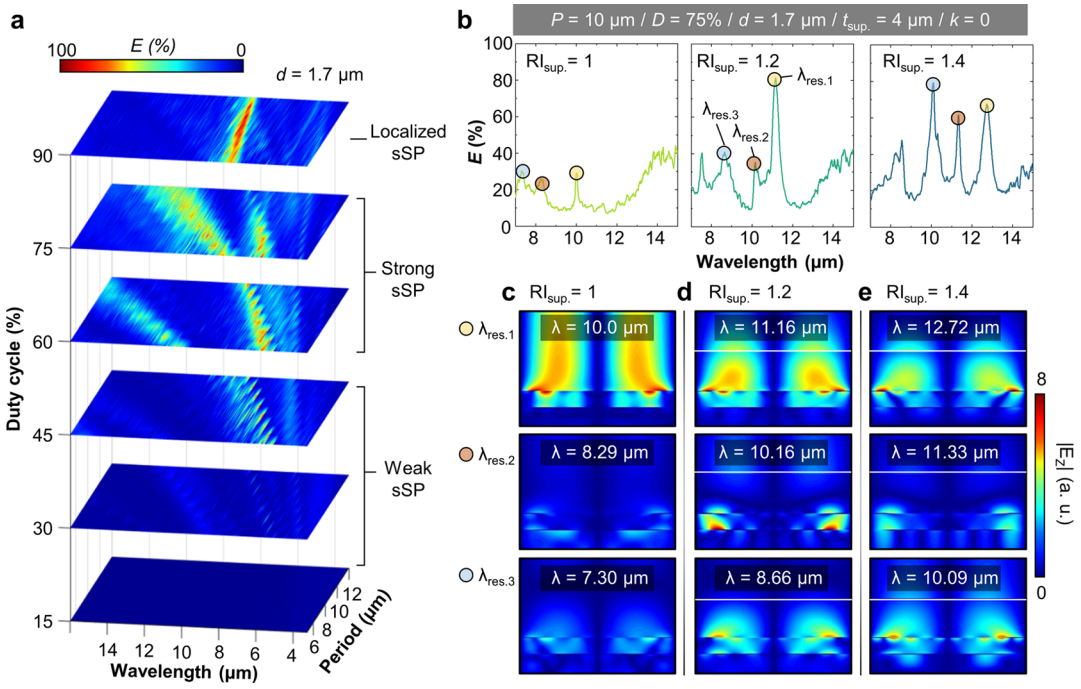

Figure 2. Analyses of a spatially selective emitter. (a) Emissivity contour plots of HTE without a superstrate layer as a function of wavelength, period, and duty cycle. The depth d is 1.7 μm. (b) Emissivity spectra of HTEs with different RI encapsulation layers (i.e., $RI_{sup.}$ = 1, 1.2, and 1.4). The extinction coefficient, k, is set to zero. Main resonant wavelengths are marked by yellow, orange, and blue circles. (c–e) Electric field distributions for three $RI_{sup.}$. (c) $RI_{sup.}$ = 1, (d) 1.2, and (e) 1.4 at each resonant wavelength. The white lines indicate the interface of superstrate layers.

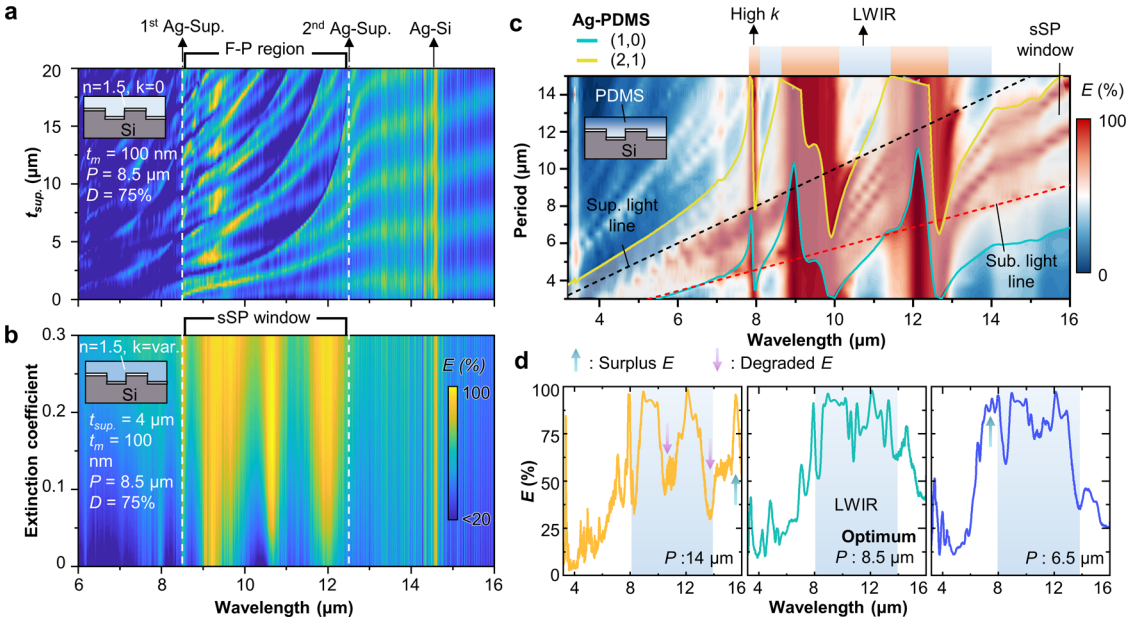

Figure 3. Analysis of the HTE with an IR-opaque superstrate for a spectrally selective emitter. (a) Emissivity contour plot of the HTE with an IR nonabsorbing layer as a function of wavelength and layer thickness ($t_{sup.}$). Two Ag-Sup. modes and one Ag-Si mode exist. The spectral domain between the two Ag-Sup. modes defines the F-P region. (b) Emissivity enhancement between superstrate modes (i.e., within the sSP window) with small extinction coefficients. The substrate mode, Ag-Si, shows sharp resonances regardless of the extinction coefficient. (c) Contour plot of PDMS-based HTE emissivity as a function of period and wavelength. The sky-blue and yellow solid lines indicate sSP at the interface of PDMS–Ag in the (1,0) and (2,1) modes, respectively. The sSP window is defined as the region between the two sSP dispersion curves, which is the shaded area. The sSP window contains four sSP resonance modes due to Ag–PDMS. The emissivity refinement is not found outside the light lines. The detailed dispersion curves are shown in Figure S3. (d) Emissivity spectra of three HTEs with different periods: (top) P = 14 μm, (middle) P = 8 μm, and (bottom) P = 6.5 μm. For all periods, $t_{sup.}$ is set to 4 μm.

HTE (Figure 1h). The fabrication process is described in detail in Section 2.2.

2.1.2. Analyses and Design of Spatially Selective HTE. The geometrical effects of various structural parameters such as the

https://dx.doi.org/10.1021/acsami.0c13177
ACS Appl. Mater. Interfaces 2020, 12, 53206–53214

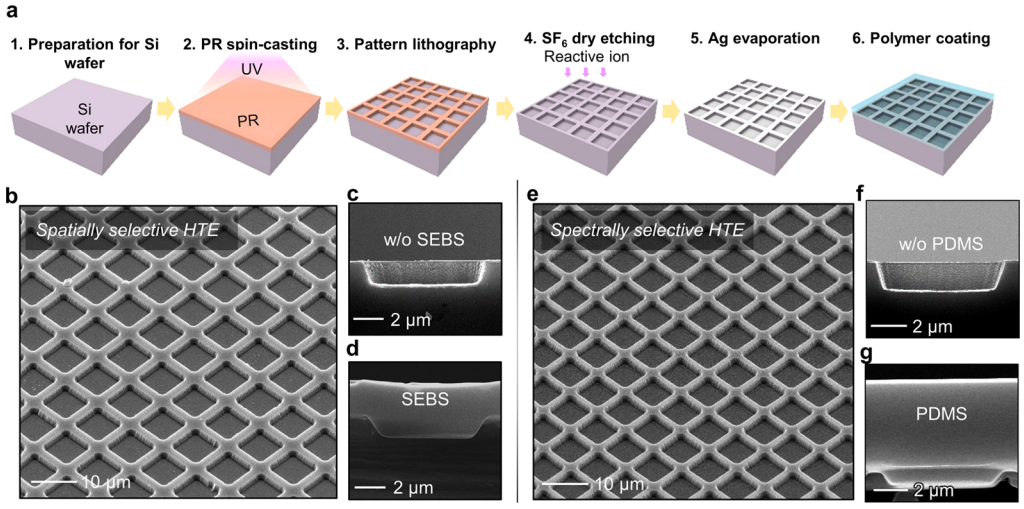

Figure 4. Fabrication process and SEM characterization of HTEs. (a) Fabrication process for HTEs using the MEMS methods. (b) Tilted SEM image of a spatially selective HTE without an IR-transparent layer (i.e., SEBS). (c,d) Cross-sectional SEM images of a spatially selective HTE (top) without SEBS and (bottom) with SEBS. (e) Tilted SEM image of a spectrally selective HTE without an IR-absorbing layer (i.e., PDMS). (f,g) Cross-sectional SEM images of a spectrally selective HTE (top) without PDMS and (bottom) with PDMS.

period (P), duty cycle (D), and depth (d) on HTEs without encapsulation layers (i.e., air) were theoretically studied (Figure 2a). This result shows that only the Ag grating with a low D does not act adequately as a strong thermal emitter, and that the optimum D is 60 to 75%. In addition, the Ag grating with high D (i.e., 90%) presents an almost period-independent strong thermal emission due to the localized sSP. The electric field distributions of the HTEs demonstrate differences between D of 75 and 90% (Figure S1a−1c and see Supporting Note 1 for details). Also, the localized sSP is studied depending on the depth parameter (Supporting Information Figure S1d and see Supporting Note 1 for details).

The implementation of the spatially selective HTE is based on a narrow band peak rearrangement by introducing an IR-transparent encapsulation layer. Figure 2b shows the effect of the refractive index (RI) of a superstrate layer (i.e., $RI_{sup.}$). For $RI_{sup.}$ = 1, three emissivity peaks exist marked by yellow, orange, and blue circles (i.e., $\lambda_{res.\ 1}$, $\lambda_{res.\ 2}$, and $\lambda_{res.\ 3}$), but these peaks are too weak to be captured using a thermal camera (Figure 2b; left). However, $RI_{sup.}$ of 1.2 considerably improves the emissivity peaks, especially, $\lambda_{res.\ 1}$ (Figure 2b; center). $RI_{sup.}$ of 1.4 strengthens more all the emissivity peaks (Figure 2b; right). In addition to the emissivity enhancement, the red shift of the main resonances is noted as the $RI_{sup.}$ increases. Therefore, the encapsulation layer coating simultaneously enables emissivity reinforcement and peak shifting from the outside to inside spectral region of interest.

To analyze this emissivity boosting, electric field distributions of the z component are calculated for the three peaks at resonant wavelengths (i.e., $\lambda_{res.\ 1}$, $\lambda_{res.\ 2}$, and $\lambda_{res.\ 3}$) as shown in Figure 2c−e. At $RI_{sup.}$ = 1, powerless electric field confinements are found at $\lambda_{res.\ 2}$ and $\lambda_{res.\ 3}$ (Figure 2c; middle and bottom). Although a strong electric field is observed at $\lambda_{res.\ 1}$, the field is considerably elongated, which indicates weak resonance (Figure 2c; top). However, the introduction of $RI_{sup.}$ = 1.2 and 1.4 leads to light confinement within the encapsulation layers (Figure 2d,e). In particular, at $\lambda_{res.\ 1}$, the vertically elongated electric field becomes shorter and at $\lambda_{res.\ 2}$ and $\lambda_{res.\ 3}$, the electric field resonances are stronger than that of $RI_{sup.}$ = 1.

2.1.3. Analysis and Design of Spectrally Selective HTE. A simple HTE with a superstrate and a constant refractive index of 1.5 and a zero extinction coefficient (Figure 3a) was studied for the design of a spectrally selective emitter. In general, spectrally restricted Fabry−Perot (F-P) resonances emerge within the superstrate sSP modes depending on the superstrate thickness.[40] Our results also exhibit the same resonance tendency: F-P resonances are only formed between two superstrate modes (i.e., 1st and 2nd Ag-Sup.), which is marked as the "F-P region" (Figure 3a; white dashed line). The electric field distributions are plotted at six points for a more thorough analysis (Figure S2 and see Supporting Note 2 for details). Interestingly, within the F-P region, the HTE with an encapsulation layer having a small extinction coefficient provides an intense emissivity enhancement, thus the F-P region is called the "sSP window" (Figure 3b). Outside the sSP window, a strong resonance peak exists only at the substrate sSP resonant wavelength. Matching the sSP window with a region of a low extinction coefficient allows the design of a selective thermal emitter with a wide spectral range.

Using the sSP window, a practical design for spectrally selective HTEs in the LWIR window is performed with a 4 μm-thick PDMS encapsulation layer as a function of period and wavelength (Figure 3c). Also, modal analysis of a PDMS-based spectrally selective HTE is performed using the sSP grating equation[41]

$$\lambda_{o,sup.} \approx \frac{P}{\sqrt{m^2 + l^2}} \sqrt{\varepsilon_{superstrate}} \quad (1)$$

$$\lambda_{o,sub.} \approx \frac{P}{\sqrt{m^2 + l^2}} \sqrt{\varepsilon_{substrate}} \quad (2)$$

where m and l are the grating orders and $\varepsilon_{substrate}$ and $\varepsilon_{superstrate}$ are the dielectric constants of the substrate and superstrate, respectively. In Figure 3c, the sky-blue and yellow solid lines denote the envelope of the sSP window that results from sSP resonances with different grating orders, such as the (1,0), (1,1), (2,0), and (2,1) orders, at the PDMS−Ag interfaces. In other words, the spectral region between the PDMS−Ag sSP modes constitutes the sSP window. The dispersion curve for

https://dx.doi.org/10.1021/acsami.0c13177
ACS Appl. Mater. Interfaces 2020, 12, 53206−53214

each mode is displayed in Figure S3. Owing to the abnormal dispersion of PDMS (see Figure S4 for the detailed optical constants of PDMS), the refractive index fluctuates significantly and the sSP resonant wavelengths shuttle up and down with the variation of the period in the weak absorption regimes of the thin PDMS. These results show that the emissivity amelioration does not require major modes of sSP, which dominantly improve the emissivity. The core factor for the refinement of emissivity overlaps with the spectral range having a weak extinction coefficient and an sSP window region.

The sSP window due to such unusual sSP dispersion covers the low absorption range of bare PDMS. Hence, it enhances the low emissivity to up to near-unity even when low extinction coefficients are used. In addition, the sSP resonances do not improve the emissivity outside the light lines. In other words, without PDMS encapsulation, emissivity enhancements are not observed between the sSP resonances (Figure S5). Figure 3d presents the surplus, degraded, and optimum emissivity by the sSP window for the three periods. At shorter periods (e.g., P = 6.5 μm), the sSP window is positioned from 6 to 8 μm (i.e., between two modes); hence, the emissivity enhancement undesirably occurs (Figure 3d; right). In contrast, the HTE with P = 14 μm shows degradation of the LWIR emissivity owing to the absence of an sSP window, but undesired emissivity enhancement occurs outside the LWIR window (Figure 3d; right). The optimum HTE with P = 8.5 μm exhibits a near-ideal spectrally selective emitter fitting within the LWIR window (Figure 3d; center).

2.2. Fabrication and Characterization of Spectrally and Spatially Selective HTEs. Figure 4a shows the schemes of fabrication steps for HTEs. At first, a silicon substrate was cleaned using acetone, isopropanol alcohol (IPA), and deionized (DI) water by sonication for 5 min (Figure 4a; Step 1). Then, a positive photoresist (PR; AZ5214 E, MicroChemicals, Germany) was spin-coated at 4000 rpm for 40 s on the silicon substrate. The sample was then baked on a hot plate at 110 °C for 60 s (soft baking). For photolithography, a mask aligner (M100, Prowin, Korea) was used with a patterned mask for the HTE under an exposure intensity of 51 mW/cm^2 for 4 s (Figure 4a; Step 2). Subsequently, the UV-exposed sample was developed in a developer (AZ-MIF-300, MicroChemicals, Germany) for 60 s (Figure 4a; Step 3). Except for the PR-masked area, an approximately 1.7 μm-thick silicon layer was etched using an inductively coupled plasma spectrometer (ICP180, Oxford Instruments, UK) for 7 min using SF_6 gas (50 sccm) under a pressure of 4 mTorr and an RF power of 50 W (Figure 4a; Step 4). After Si etching, the PR mask was removed using an acetone bath for 5 min. A 100 nm-thick Ag layer was then deposited using an electron beam evaporator (KVE-E2000, Korea Vacuum Tech Ltd., Korea) at a rate of approximately 1 Å/s (Figure 4a; Step 5). After the Ag deposition process, the encapsulation layers (i.e., PDMS and styrene−ethylene−butylene−styrene; SEBS) were spin-coated on the Ag-coated silicon groove (Figure 4a; Step 6).

The fabricated spatially selective HTE is shown in Figure 4b. The geometrical parameters of the fabricated sample are P = 10 μm, d = 1.7 μm, D = 75%, $t_{sub.}$ = 500 μm, and t_{metal} = 100 nm. Figure 4c displays the width and etched depth of the sample. For spin-casting of SEBS, SEBS beads (Tuftec H1062, Asahi Kasei, Japan) and a chloroform solvent (C2432, Sigma-Aldrich) were mixed at a weight percent of 3.3 to 96.7 in a test tube at room temperature. The solution was then sonicated for a day to completely dissolve the SEBS beads. After the complete dissolution of SEBS in the solvent, the SEBS solution was spin-coated at 3000 rpm for 30 s on the Ag-coated silicon groove. The spin-casted SEBS layer on the Ag groove has ∼3 μm thickness (Figure 4d).

The SEM image of the fabricated spectrally selective HTE is also shown (Figure 4e). The geometrical parameters of the fabricated sample are P = 8.5 μm, d = 1.7 μm, D = 75%, t_{sub} = 500 μm, and t_{metal} = 100 nm. The cross-sectional SEM image displays the obtained structure (Figure 4f). PDMS (Sylgard 184, Dow Corning, USA) was mixed with a base/agent ratio of 10:1 and degassed to remove air bubbles. The PDMS solution was spin-coated on the Ag-coated silicon groove at 8000 rpm for 50 s. Finally, the spin-coated sample was cured on a hot plate at 120 °C for 7 min, and the obtained PDMS thickness was ∼7 μm (Figure 4g).

2.3. Demonstrations of Spatially and Spectrally Selective HTEs. *2.3.1. Infrared Data Encoding/Decoding Using Spatially Selective HTE.* The fabricated spatially selective HTE with SEBS is utilized for the demonstration of infrared data encoding and decoding. Figure 5a illustrates the

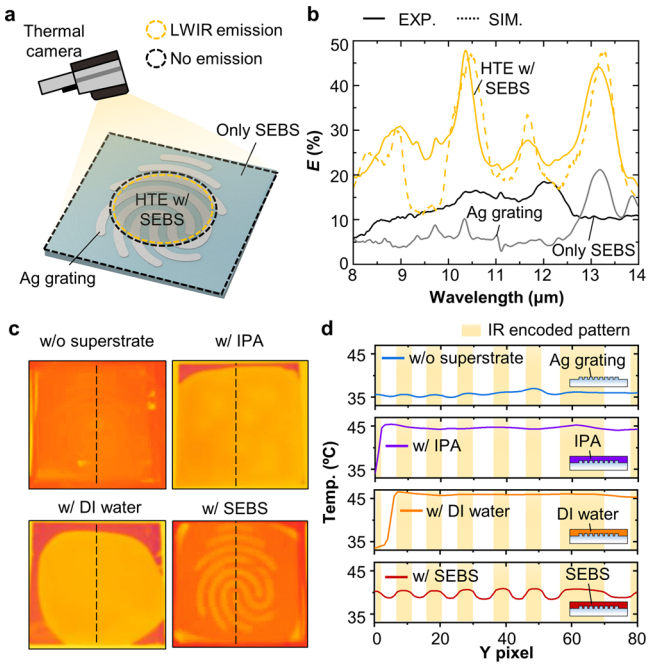

Figure 5. Demonstration of a spatially selective HTE. (a) Schematic illustration of infrared data encoding using an HTE with SEBS coating. "Ag grating" and "only SEBS" areas have weak emissivity indicating that they are IR-invisible. (b) Measured and simulated emissivity spectra of HTE, Ag grating, and only SEBS (approximately 3 μm). (c) Thermal images of four cases: w/o superstrate (i.e., only patterned Ag grating), HTE with IPA, DI water, and SEBS coatings. In "w/ SEBS", a fingerprint pattern is observed. (d) Cross-sectional contrast in four thermal images. The observation line is denoted by a black dashed line in (c). Insets display the schematics of cross-sectional layouts of the sample.

experimental procedure. Because a thin SEBS film is IR-transparent (Figure 5b; black solid curve), only the SEBS area is thermally invisible. Also, the Ag grating area has weak emissivity (Figure 5b; gray solid line); hence, it is barely IR-visible. In contrast, the HTE with SEBS exhibits enhanced emissivity due to the intertwined sSP (Figure 5b; yellow lines).

https://dx.doi.org/10.1021/acsami.0c13177
ACS Appl. Mater. Interfaces 2020, 12, 53206−53214

Therefore, in the experiment, a thermal camera may detect a hidden pattern, fingerprint, only in the case of HTE with SEBS. For various control groups, four cases are considered as follows: without SEBS (i.e., air), with IPA, with DI water, and with SEBS. The constant refractive index and the zero extinction coefficient might be a cause of a little mismatch between the simulation and the measurement.

Thermal imaging results demonstrate the abovementioned hypotheses (Figure 5c). Without a superstrate (i.e., only a patterned Ag grating), a fingerprint pattern could not be observed due to low emissivity, and with IPA and DI water, high emission of the solvents hinders the achievement of a patterned image. However, with SEBS, the sample clearly shows a fingerprint pattern. Figure 5d shows the quantitatively evaluated acquired temperatures for these four cases along the vertical black dashed lines shown in Figure 5c. This result suggests that the patterned Ag grating sample has a low contrast temperature profile. Also, the patterned Ag grating is largely influenced by ambient thermal radiation because of its high reflectivity. The cases of IPA and DI water cannot present a noticeable pattern owing to their high emissivity, and the HTE with SEBS provides a distinguishable IR-encoded pattern resulting from the apparent emissivity difference between the Ag patterned area and the no patterned area. Figure S6 shows the areas of the patterned Ag grating and bare Ag and the spatially different emissions depending on the superstrates. The PDMS encapsulation layer cannot offer a classifiable thermal image (Figure S7). The variation of duty cycle, D, enhances the contrast between the thermally visible and invisible areas (Figure S8). Additional advantages of SEBS include acting as an optical curtain for concealing the IR-encoding pattern (Figure S9) and erasability by simply immersing in a solvent (Figure S10). Owing to this feature, the HTE with SEBS facilitates IR data encoding and decoding. The detailed measurement steps are explained in the Section 4.

2.3.2. Near-Unity Selective Emitter for Radiative Cooling Using Spectrally Selective HTE. A near-unity and selectively wideband LWIR emission can be used for radiative cooling applications. Radiative cooling lowers the temperature of the objects by radiative heat transfer through an LWIR window to the universe (Figure S11). In this context, the fabricated spectrally selective HTE is most useful to cool objects (Figure 6a). As control groups, Ag grating (i.e., absence of a superstrate) and thin PDMS film (i.e., only PDMS) samples are prepared. Figure 6b shows the measured emissivity spectra of the Ag grating, only PDMS, and HTE with PDMS. The simulated emissivity spectra coincide with the measurement results. These results demonstrate that PDMS encapsulation of the HTE improves the LWIR-matching selective emission.

Based on humidity or cloud status, the LWIR opacity varies. For instance, a clear day has a transparent LWIR window, but a humid or cloudy day has an opaque LWIR window. In this case, the opacity of the LWIR window should be considered to estimate the cooling performance of samples. To evaluate the cooling performance of the fabricated samples, the energy balance was analyzed using the thermal equilibrium equation[15]

$$P_{rad}(T_{sample}) - P_{Sun} - P_{atm}(T_{ambient}) + h_c(T_{sample} - T_{ambient}) = 0 \quad (3)$$

where $P_{rad}(T_{sample})$ is the radiative power of the sample per unit area, $P_{atm}(T_{ambient})$ is the absorbed power from the atmosphere per unit area, P_{Sun} is the solar power absorbed by the sample

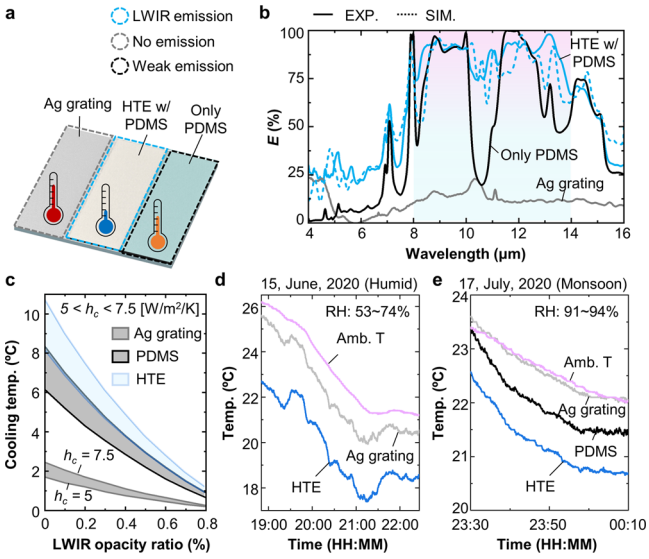

Figure 6. Demonstration of a spectrally selective HTE. (a) Schematic illustration of radiative cooling using an HTE with a PDMS coating. "Ag grating" and "only PDMS" areas have relatively weak emissivity; thus, these act as control groups. (b) Measured and simulated emissivity spectra of the HTE, Ag grating, and only PDMS samples. (c) Calculated cooling temperature of three cases as a function of LWIR opacity based on the thermal equilibrium equation. The nonradiative heat transfer coefficient, h_c, ranges from 5 to 7.5 W/m^2/K for a practical situation. (d,e) Logged temperatures of (d) HTE and Ag grating samples in a humid day and (e) all samples in the monsoon season.

per unit area, and $h_c(T_{sample} - T_{ambient})$ is the nonradiative heat exchange power including conduction and convection. The four power terms are explained in detail in the Section 4.

Figure 6c shows the cooling temperature (i.e., $T_{ambient} - T_{sample}$) in terms of the LWIR window opacity ratio and nonradiative heat exchange coefficient, h_c. The cooling temperatures for the three samples are in the range of $5 < h_c < 7.5$ W m^{-2} K^{-1}. This result theoretically supports the conclusion that the cooling performance of the HTE with PDMS encapsulation exceeds the other two samples under any weather conditions. For a representative LWIR window case considering clear and humid weather conditions, cooling performances were calculated in terms of the cooling temperature and power in detail (Figure S12).

The logged temperature results of the samples demonstrate that the HTE with PDMS encapsulation has an exceptionally increased cooling capability of ~4 °C subambient cooling due to the highly selective strong emission in a humid day (Figure 6d). The measured results match well with the simulated cooling temperatures at h_c = 7.5 W m^{-2} K^{-1} and LWIR opacity ratio = 0.5 for both the Ag grating and HTE with PDMS. In addition, the three samples were compared simultaneously in a monsoon season (Figure 6e), which is extremely humid (relative humidity; RH: 91 − 94%). In this result, the HTE with PDMS also demonstrates the most effective cooling performance, and the results match with the simulated cooling temperature at h_c = 5 W m^{-2} K^{-1} and LWIR opacity ratio = 0.8. Based on these calculation and measurement results, the HTE with PDMS definitely is superior to other samples in a clear day. Moreover, the selective emitter has advantages such as thermoregulation in the winter season and efficient cooling in urban areas because of its low absorption of ambient

https://dx.doi.org/10.1021/acsami.0c13177
ACS Appl. Mater. Interfaces 2020, 12, 53206−53214

radiation.[42] Also, replacing with a solar-transparent substrate theoretically permits daytime radiative cooling (Figure S13). The measurement details are explained in the Section 4.3.

3. CONCLUSIONS

In this work, we presented spatially and spectrally selective emitters based on polymer hybrid spoof plasmonics and their applications. Our IR emitter can function in these two modes with the encapsulation of IR-transparent or IR-opaque polymers such as SEBS or PDMS, respectively. Spectral and modal analyses of the sSP resonance provide a design rule for optimum HTEs. Based on the deduced design guidelines, we fabricated HTEs with spatially resolved emission peaks in specific areas and selective/wide near-unity emission within the LWIR window. Finally, IR data encoding/decoding and radiative cooling were demonstrated in these samples. The IR encoding/decoding device can reveal and hide thermally viewable data through coating and erasing a thin SEBS layer. The radiative cooling device can significantly lower the object temperature. These successful demonstrations show that the proposed HTE is a powerful tool to tailor IR emission in a spatially and spectrally selective manner.

4. EXPERIMENTAL SECTION

4.1. Optical Simulation. A rigorous coupled-wave analysis-based commercial software (DiffractMOD, RSoft Design Group, Synopsys, USA) was utilized to simulate the emissivity spectra in the IR range. Electric field distributions were also calculated using this tool. In all the simulations, a 0.1 nm square grid size and five harmonics were used to numerically calculate the stable emissivity. Complex refractive index dispersions for Si and PDMS were considered to obtain accurate spectral results. The refractive indices were obtained from previously published results.[43] In the simulation of SEBS, a constant refractive index of 1.5 and a zero extinction coefficient were exploited to mimic an IR-transparent layer. The Drude model was used for the optical constants of Ag.

4.2. Characterization. The emissivity spectra were characterized by measuring the reflectance spectra of the samples using a Fourier transform infrared spectrometer (Spectrum Paragon, PerkinElmer, Inc., USA) with an Au-coated integrating sphere to capture the diffracted light. The infrared rays cannot pass through even a thin Ag layer; hence, the emissivity spectra were derived from the measured reflectance spectra (i.e., E = 1 − R). A scanning electron microscope (SEM; S-4700, Hitachi Hi-Technologies, Japan) was used to observe the HTE structures.

For the thermally encoded data measurement, the fabricated HTE was placed on a hot plate at 50 °C before and after the SEBS coating for supplying heat to the sample uniformly. The detailed encoded pattern is shown in Figure S6a. A thermal camera (E6, FLIR Systems, Inc., USA) captured the sample surface. For the radiative cooling temperature measurement, the back surfaces of the samples were laminated with Cu foils of the same size as the samples. Between the samples and Cu foils, adhesive temperature sensors (ST-50, RKC Instrument Inc., Japan) were inserted and connected to a data logger (RDXL6SD, Omega Engineering, USA). An ambient air sensor was inserted in an Al box with air flow to measure the temperature of the naturally convective air.

4.3. Thermal Equilibrium Equation. The thermal equilibrium equation, $P_{rad}(T_{sample}) - P_{Sun} - P_{atm}(T_{ambient}) + P_{non-radi} = 0$, is composed of the following four terms

$$P_{rad}(T_{sample}) = \int_0^{2\pi}\int_0^{\pi/2}\int_0^{\infty} I_{BB}(T_{sample}, \lambda)\, \varepsilon(\lambda, \theta)\cos(\theta)\sin(\theta)\,d\lambda\,d\theta\,d\phi \quad (4)$$

$$P_{atm}(T_{ambient}) = \int_0^{2\pi}\int_0^{\pi/2}\int_0^{\infty} I_{BB}(T_{ambient}, \lambda)\, \varepsilon(\lambda, \theta)\varepsilon_{amb}(\lambda, \theta)\cos(\theta)\sin(\theta)\,d\lambda\,d\theta\,d\phi \quad (5)$$

$$P_{sun} = \int_0^{\infty} I_{AM1.5G}(\lambda)\varepsilon(\lambda, \theta)\,d\lambda \quad (6)$$

$$P_{non-radi} = h_c(T_{sample} - T_{ambient}) \quad (7)$$

Here, $I_{BB} = (2hc^2/\lambda^5)/[e^{hc/\lambda k_B T} - 1]$ is the spectral radiance of a blackbody at temperature T, where h, c, k_B, λ, and h_c are the Planck's constant, the velocity of light, the Boltzmann constant, the wavelength, and the nonradiative heat exchange coefficient, respectively. The atmospheric emissivity is given by $\varepsilon_{amb}(\lambda, \theta) = 1 - t(\lambda)^{1/\cos(\theta)}$, where t is the sky transmission calculated by MODTRAN 6 using the conditions of an urban site at midlatitude in summer. We did not consider P_{Sun} for the comparison of the LWIR radiative powers.

■ ASSOCIATED CONTENT

Supporting Information

The Supporting Information is available free of charge at https://pubs.acs.org/doi/10.1021/acsami.0c13177.

Electric field analyses on Ag grating; parametric study for localized sSP; electric field analyses on spectrally selective HTE; dispersion curves of sSP resonances; complex refractive indices of PDMS; emissivity contour plot of HTE under various conditions; thermal data encoding/decoding test on HTE with PDMS; high-performance spatially selective HTE with SEBS; thermally encoded data pattern information; erasability test of SEBS; illustration of the principle of radiative cooling; estimated cooling performances; and evaluation of applicability of daytime radiative cooling (PDF)

■ AUTHOR INFORMATION

Corresponding Author

Young Min Song − *School of Electrical Engineering and Computer Science (EECS), Anti-Virus Research Center, and AI Graduate School, Gwangju Institute of Science and Technology (GIST), Gwangju 61005, Republic of Korea;* orcid.org/0000-0002-4473-6883; Email: ymsong@gist.ac.kr

Authors

Gil Ju Lee − *School of Electrical Engineering and Computer Science (EECS), Gwangju Institute of Science and Technology (GIST), Gwangju 61005, Republic of Korea;* orcid.org/0000-0003-2225-2738

Do Hyeon Kim − *School of Electrical Engineering and Computer Science (EECS), Gwangju Institute of Science and Technology (GIST), Gwangju 61005, Republic of Korea;* orcid.org/0000-0003-3060-1192

Se-Yeon Heo − *School of Electrical Engineering and Computer Science (EECS), Gwangju Institute of Science and Technology (GIST), Gwangju 61005, Republic of Korea*

Complete contact information is available at: https://pubs.acs.org/10.1021/acsami.0c13177

Author Contributions

‖G.J.L. and D.H.K. equally contributed to this work. All authors have given approval to the final version of the manuscript.

https://dx.doi.org/10.1021/acsami.0c13177
ACS Appl. Mater. Interfaces 2020, 12, 53206−53214

Notes

The authors declare no competing financial interest.

■ ACKNOWLEDGMENTS

This work was supported by the National Research Foundation of Korea (NRF-2020R1A2C2004983/NRF-2018M3D1A1058997/NRF-2018R1A4A1025623). This work was also supported by the GIST Research Institute (GRI) grant funded by the GIST in 2020 and the Korea Institute of Energy Technology Evaluation and Planning (KETEP) and by the Ministry of Trade, Industry, and Energy (MOTIE) of the Republic of Korea (Grant No. 20183010014310). G.J.L. acknowledges the support from the NRF (NRF-2017H1A2A1042138). This work was partly supported by Institute of Information & communications Technology Planning & Evaluation (IITP) grant funded by the Korea government(MSIT) (No.2020-0-01000, Light field and LiDAR sensor fusion systems for full self-driving).

■ REFERENCES

(1) Swanson, R. M. A Proposed Thermophotovoltaic Solar Energy Conversion System. *Proc. IEEE* **1979**, *67*, 446−447.
(2) Lin, S. Y.; Moreno, J.; Fleming, J. G. Three-dimensional Photonic-crystal Emitter for Thermal Photovoltaic Power Generation. *Appl. Phys. Lett.* **2003**, *83*, 380−382.
(3) Sai, H.; Yugami, H. Thermophotovoltaic Generation with Selective Radiators Based on Tungsten Surface Gratings. *Appl. Phys. Lett.* **2004**, *85*, 3399−3401.
(4) Rephaeli, E.; Fan, S. Absorber and Emitter for Solar Thermophotovoltaic Systems to Achieve Efficiency Exceeding the Shockley−Queisser Limit. *Opt. Express* **2009**, *17*, 15145−15159.
(5) Chan, W. R.; Bermel, P.; Pilawa-Podgurski, R. C. N.; Marton, C. H.; Jenson, K. F.; Senkevich, J. J.; Joannopoulos, J. D.; Soljačić, M.; Celanovic, I. Toward High-energy-density, High-efficiency, and Moderate-temperature Chip-scale Thermophotovoltaics. *Proc. Natl. Acad. Sci. U. S. A.* **2013**, *110*, 5309−5314.
(6) Meléndez, J.; de Castro, A. J.; López, F.; Meneses, J. Spectrally Selective Gas Cell for Electrooptical Infrared Compact Multigas Sensor. *Sens. Actuators A* **1995**, *47*, 417−421.
(7) Werle, P.; Slemr, F.; Maurer, K.; Kormann, R.; Mücke, R.; Jänker, B. Near- and Mid-Infrared Laser-optical Sensors for Gas Analysis. *Opt. Lasers Eng.* **2002**, *37*, 101−114.
(8) Rubio, R.; Santander, J.; Fonseca, L.; Sabaté, N.; Gràcia, I.; Cané, C.; Udina, S.; Marco, S. Non-selective NDIR Array for Gas Detection. *Sens. Actuators, B* **2007**, *127*, 69−73.
(9) Hodgkinson, J.; Tatam, R. P. Optical Gas Sensing: A Review. *Meas. Sci. Technol.* **2013**, *24*, No. 012004.
(10) Rodrigo, D.; Limaj, O.; Janner, D.; Etezadi, D.; de Abajo, F. J. G.; Pruneri, V.; Altug, H. Mid-infrared Plasmonic Biosensing with Graphene. *Science* **2015**, *349*, 165−168.
(11) Cielo, P.; Lewak, R.; Balageas, D. Thermal Sensing for Industrial Quality Control. *Proc. SPIE* **1986**, *581*, 47−54.
(12) Li, D.; Li, Y.; Su, Y.; Chi, C.; Huang, B. Atmospheric-window-matching Hierarchical Broadband Infrared Absorber Realized by Lithography-free Fabrication. *Front. Energy Res.* **2018**, *6*, 20.
(13) Zhang, J.; Wei, R.; ElKabbash, M.; Campbell, E. M.; Guo, C. Thin-film Perfect Infrared Absorbers over Single- and Dual-band Atmospheric Windows. *Opt. Lett.* **2020**, *45*, 2800−2803.
(14) Sofradir-EC, Inc., LWIR or MWIR infrared imaging: which is best for your application?, https://www.lynred-usa.com/media/wp-lwir-or-mwir-infrared-imaging-v01-web.pdf.
(15) Lee, G. J.; Kim, Y. J.; Kim, H. M.; Yoo, Y. J.; Song, Y. M. Colored, Daytime Radiative Coolers with Thin-film Resonators for Aesthetic Purposes. *Adv. Opt. Mater.* **2018**, *6*, 1800707.
(16) Chen, Z.; Zhu, L.; Raman, A.; Fan, S. Radiative Cooling to Deep Sub-freezing Temperatures through A 24-h Day-night Cycle. *Nat. Commun.* **2016**, *7*, 13729.
(17) Zeyghami, M.; Goswami, D. Y.; Stefanakos, E. A Review of Clear Sky Radiative Cooling Developments and Applications in Renewable Power Systems and Passive Building Cooling. *Sol. Energy Mater. Sol. Cells* **2018**, *178*, 115−128.
(18) Heo, S.-Y.; Lee, G. J.; Kim, D. H.; Kim, Y. J.; Ishii, S.; Kim, M. S.; Seok, T. J.; Lee, B. J.; Lee, H.; Song, Y. M. A Janus Emitter for Passive Heat Release from Enclosures. *Sci. Adv.* **2020**, *6*, 36.
(19) Franklin, D.; Modak, S.; Vazquez-Guardado, A.; Safaei, A.; Chanda, D. Covert Infrared Image Encoding Through Imprinted Plasmonic Cavities. *Light Sci. Appl.* **2018**, *7*, 93.
(20) Xu, Z.; Li, Q.; Du, K.; Long, S.; Yang, Y.; Cao, X.; Luo, H.; Zhu, H.; Ghosh, P.; Shen, W.; Qiu, M. Spatially Resolved Dynamically Reconfigurable Multilevel Control of Thermal Emission. *Laser Photonics Rev.* **2019**, *14*, 1900162.
(21) Makhsiyan, M.; Bouchon, P.; Jaeck, J.; Pelouard, J.-L.; Haidar, R. Shaping the Spatial and Spectral Emissivity at The Diffraction Limit. *Appl. Phys. Lett.* **2015**, *107*, 251103.
(22) Fleming, J. G.; Lin, S. Y.; El-Kady, I.; Biswas, R.; Ho, K. M. All Metallic Three-dimensional Photonic Crystals with A Large Infrared Bandgap. *Nature* **2002**, *417*, 52−55.
(23) Pralle, M. U.; Moelders, N.; McNeal, M. P.; Puscasu, I.; Greenwald, A. C.; Daly, J. T.; Johnson, E. A.; George, T.; Choi, D. S.; El-Kady, I.; Biswas, R. Photonic Crystal Enhanced Narrow-band Infrared Emitters. *Appl. Phys. Lett.* **2002**, *81*, 4685−4687.
(24) Rinnerbauer, V.; Yeng, Y. X.; Chan, W. R.; Senkevich, J. J.; Joannopoulos, J. D.; Soljačić, M.; Celanovic, I. High-temperature Stability and Selective Thermal Emission of Polycrystalline Tantalum Photonic Crystals. *Opt. Express* **2013**, *21*, 11482−11491.
(25) Park, S.-J.; Kim, Y.-B.; Moon, Y.-J.; Cho, J.-W.; Kim, S.-K. Tuning of Polarized Room-temperature Thermal Radiation Based on Nanogap Plasmon Resonance. *Opt. Express* **2020**, *28*, 15472−15481.
(26) Chang, Y.; Yao, J.; Wu, X.; Wu, D.; Liu, X. Strong and Weak Couplings in Molecular Vibration-plasmon Hybrid Structures. *Opt. Express* **2019**, *27*, 1479−1487.
(27) Pendry, J. B.; Holden, A. J.; Robbins, D. J.; Stewart, W. J. Magnetism from Conductors and Enhanced Nonlinear Phenomena. *IEEE Trans. Microwave Theor. Tech.* **1999**, *47*, 2075−2084.
(28) Landy, N. I.; Sajuyigbe, S.; Mock, J. J.; Smith, D. R.; Padilla, W. J. Perfect Metamaterial Absorber. *Phys. Rev. Lett.* **2008**, *100*, 207402.
(29) Liu, X.; Starr, T.; Starr, A. F.; Padilla, W. J. Infrared Spatial and Frequency Selective Metamaterial with Near-unity Absorbance. *Phys. Rev. Lett.* **2010**, *104*, 207403.
(30) Aydin, K.; Ferry, V. E.; Briggs, R. M.; Atwater, H. A. Broadband Polarization-independent Resonant Light Absorption using Ultrathin Plasmonic Super Absorbers. *Nat. Commun.* **2011**, *2*, 517.
(31) Liu, X.; Tyler, T.; Starr, T.; Starr, A. F.; Jokerst, N. M.; Padilla, W. J. Taming The Blackbody with Infrared Metamaterials as Selective Thermal Emitters. *Phy. Rev. Lett.* **2011**, *107*, No. 045901.
(32) Yang, Z.-Y.; Ishii, S.; Yokoyama, T.; Dao, T. D.; Sun, M.-G.; Pankin, P. S.; Timofeev, I. V.; Nagao, T.; Chen, K.-P. Narrowband Wavelength Selective Thermal Emitters by Confined Tamm Plasmon Polaritons. *ACS Photonics* **2017**, *4*, 2212−2219.
(33) Cui, Y.; He, Y.; Jin, Y.; Ding, F.; Yang, L.; Ye, Y.; Zhong, S.; Lin, Y.; He, S. Plasmonic and Metamaterial Structures as Electromagnetic Absorbers. *Laser Photonics Rev.* **2014**, *8*, 495−520.
(34) Raman, A. P.; Anoma, M. A.; Zhu, L.; Rephaeli, E.; Fan, S. Passive Radiative Cooling Below Ambient Air Temperature Under Direct Sunlight. *Nature* **2014**, *515*, 540−544.
(35) Hossain, M. M.; Jia, B.; Gu, M. A Metamaterial Emitter for Highly Efficient Radiative Cooling. *Adv. Opt. Mater.* **2015**, *3*, 1047−1051.
(36) Cui, Y.; Fung, K. H.; Xu, J.; Ma, H.; Jin, Y.; He, S.; Fang, N. X. Ultrabroadband Light Absorption by A Sawtooth Anisotropic Metamaterial Slab. *Nano Lett.* **2012**, *12*, 1443−1447.
(37) Lochabaum, A.; Fedoryshyn, Y.; Dorodnyy, A.; Koch, U.; Hafner, C.; Leuthold, J. On-chip Narrowband Thermal Emitter for Mid-IR Optical Gas Sensing. *ACS Photonics* **2017**, *4*, 1371−1380.

https://dx.doi.org/10.1021/acsami.0c13177
ACS Appl. Mater. Interfaces 2020, 12, 53206−53214

(38) Wang, Z.; Clark, J. K.; Huang, L.-C.; Ho, Y.-L.; Delaunay, J.-J. Plasmonic Nanochannel Structure for Narrow-band Selective Thermal Emitter. *Appl. Phys. Lett.* **2017**, *110*, 251102.
(39) Moridani, A. K.; Zando, R.; Xie, W.; Howell, I.; Watkins, J. J.; Lee, J.-H. Plasmonic Thermal Emitters for Dynamically Tunable Infrared Radiation. *Adv. Opt. Mater.* **2017**, *5*, 1600993.
(40) Arora, P.; Krishnan, A. Fourier Plane Colorimetric Sensing Using Broadband Imaging of Surface Plasmons and Application to Biosensing. *J. Appl. Phys.* **2015**, *118*, 233105.
(41) Gao, Z.; Wu, L.; Gao, F.; Luo, Y.; Zhang, B. Spoof Plasmonics: From Metamaterial Concept to Topological Description. *Adv. Mater.* **2018**, *30*, 1706683.
(42) Mandal, J.; Mandal, S.; Brewer, J.; Ramachandran, A.; Raman, A. P. Radiative Cooling and Thermoregulation in The Earth's Glow. 2020, arXiv:physics/2006.11931.arXiv.org e-Print archive. https://arxiv.org/abs/2006.11931 (accessed August 31, 2020).
(43) Srinivasan, A.; Czapla, B.; Mayo, J.; Narayanaswamy, A. Infrared Dielectric Function of Polydimethylsiloxane and Selective Emission Behavior. *Appl. Phys. Lett.* **2016**, *109*, No. 061905.

https://dx.doi.org/10.1021/acsami.0c13177
ACS Appl. Mater. Interfaces 2020, 12, 53206−53214